Research Article | Vol. 33, No. 7 / 7 Apr 2025 / Optics Express 15304
Optics EXPRESS

Designing optical anisotropy in low-index nanolattices

VIJAY ANIRUDH PREMNATH, KWON SANG LEE, AND CHIH-HAO CHANG*

Walker Department of Mechanical Engineering, The University of Texas at Austin, Austin, TX 78712, USA
**chichang@utexas.edu*

Abstract: This research investigates the optical anisotropy and structure-induced birefringence in low-index nanolattices. By designing the unit-cell geometry using 3-dimentional (3D) colloidal lithography, nanolattices can exhibit different refractive indices along orthogonal directions due to the structure geometry. The out-of-plane and in-plane indices are characterized using spectroscopic ellipsometry and agree well with the anisotropic Cauchy material model. Exhibit positive-uniaxial birefringence, the nanolattices can have up to $\Delta n = 0.003$ for nanolattices with low indices that range from 1.04 to 1.12. The birefringence is modeled using the finite-difference-time-domain (FDTD) method, where the reflectance of an anisotropic film is calculated to iteratively solve for the indices. The theoretical model and experimental data indicate that the birefringence can be controlled by the unit-cell geometry based on the relative length scale of the particle diameter to the exposure wavelength. This work demonstrates that it is possible to precisely design optical birefringence in 3D nanolattices, which can find applications in polarizing optics, nanophotonics, and wearable electronics.

1. Introduction

The field of nanophotonics has attracted significant attention over the past two decades, with applications in augmented and virtual reality (AR/VR), advanced displays, and quantum computers [1–3]. Such nanophotonic elements are designed to manipulate light based on the geometry and material composition of nanoscale features. One particular area is metasurfaces, which are engineered nanophotonic elements with sub-wavelength features that can precisely control phase, amplitude, and polarization of light [4–6]. Recent work has demonstrated perfect absorbers [7], super-lenses [8], and polarization imaging [9], which can have applications in the field of flat optics. Another type of photonic nanostructure is photonic crystals, which have periodical index function in one, two, or three dimensions [10,11]. Photonic crystals can be integrated into elements such as ring resonators to enhance optical confinement and control of light propagation, improving resonator quality factors and enabling precise wavelength filtering in photonic circuits [12–14].

Nanophotonic elements can also induce form birefringence, which results in different effective refractive indices along orthogonal directions [15,16]. As opposed to birefringence observed in natural crystalline material [17–19], this anisotropy is caused by a variation in micro/nanoscale geometry rather than the intrinsic properties. This property is useful in applications such as wavelength-selective filters, polarizers, and wave plates, where the control of the polarization state of light is crucial. Recent work has demonstrated sub-wavelength gratings, hole arrays, and elliptical nanoparticle arrays that exhibit uniaxial birefringence [20–22]. These materials have two principal refractive indices, namely the ordinary (n_o) and extraordinary index (n_e). For instance, sub-wavelength gratings with designed duty cycle and periodicity can exhibit uniaxial birefringence of 0.225, where $n_e = 1.120$ and $n_o = 1.345$ [22]. While there have been a significant number of studies on the birefringence of 2D photonic nanostructures, optical birefringence in 3D photonic crystals have also been recently explored [23,24].

#554138 https://doi.org/10.1364/OE.554138
Journal © 2025 Received 14 Jan 2025; revised 10 Mar 2025; accepted 12 Mar 2025; published 27 Mar 2025

Optics EXPRESS

Low refractive index materials are another emerging class of optical materials, and they are essential for increasing the index contrast in nanophotonic elements [25–30]. One effective approach to achieving low indices is by fabricating nanolattices with high porosity, which have demonstrated excellent optical and mechanical properties [31–36]. Such high-stiffness, low-index nanolattice can be used as building blocks to create multilayer photonic elements such as antireflection coating and dielectric reflector [36,37]. However, in previous work these nanolattice materials have been assumed to be isotropic, which can be inaccurate depending on the unit-cell geometry. A recent study has indicated that the measured refractive index can depend on the incident angle [38], which points to potential anisotropic material behavior. Therefore, the optical anisotropy in nanolattices is not well understood and requires further investigation to fully exploit their potential in photonic applications.

In this work, we demonstrate the design, modeling, and characterization of uniaxial birefringence in ultra-low index, highly porous 3D nanolattices. The control of ordinary and extraordinary refractive indices is achieved through precise engineering of the unit-cell geometry in the in-plane and out-of-plane directions. By leveraging the unique properties of these porous structures, we enable tailored optical anisotropy and understand the relationship between lattice geometry and birefringence in low-index materials. The fabricated nanolattices characterized using spectroscopic ellipsometry using an anisotropic Cauchy material model and exhibits positive uniaxial birefringence. The nanolattices can be approximated as an anisotropic film using FDTD method, where the reflection is simulated to extract the indices using an iterative algorithm. The experimental results indicate that the birefringence scales with the anisotropy in the unit-cell geometry, which is confirmed by the simulation model. The highly porous nature and tunable optical properties of these lattices make them ideal for applications like anti-reflective coatings, optical cloaking, and polarization-sensitive elements. Our research goal is to use these lattices as low-index material for building multilayer photonic structures, such as high-efficiency Bragg reflectors with minimal layers [33]. However, understanding and controlling birefringence in these structures is critical, as uncontrolled anisotropy can degrade performance in applications requiring uniform optical properties across different polarization states. This work thereby improves the understanding of anisotropy in nanolattices and can lead to important applications in multifunctional nanostructures, nanophotonic elements, and wearable display.

2. Experimental methodology

2.1. Numerical modelling and design of anisotropic nanolattices

The geometry of a nanolattice material with isotropic and anisotropic material properties are illustrated in Fig. 1. Here the idealized isotropic nanolattice is shown on the left, which has

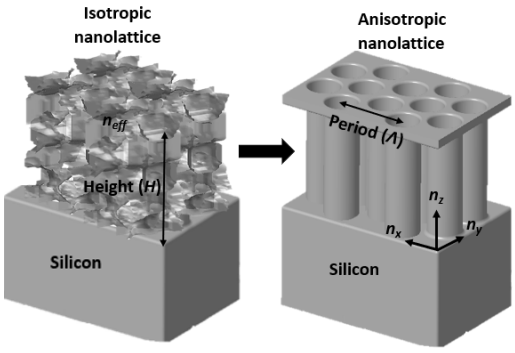

Fig. 1. Schematic of an ideal isotropic lattice with uniform periodicity in all three directions vs an anisotropic lattice with cylindrical elements.

Optics EXPRESS

a similar volume fraction of the solid phase in all three directions. On the other hand, the anisotropic nanolattices consist of cylindrical elements that are vertically aligned, which can lead to different indices along the out-of-plane (n_z) and the in-plane directions (n_x and n_y). The depolarization factor is a measure of how the electric field is distributed within the unit cell when light passes through the material. For a cylindrical unit cell, the depolarization factor will be lower along the long axis compared to the shorter axes. This is because the electric field can more easily polarize along the elongated direction, leading to a higher effective refractive index along that axis. Conversely, along the shorter axes, the depolarization factor is higher, resulting in a lower effective refractive index. As the degree of anisotropy increases, the birefringence between the orthogonal directions is expected to increase. The key geometric parameter is the unit-cell geometry of the nanolattice, which can include the period, duty-cycle, and feature width in the two directions.

The nanolattices studied in this work is fabricated using 3D colloidal phase lithography, which has been previously reported [38–40]. In this approach, self-assembled polystyrene nanospheres assembled on photoresist act as near-field phase mask for volumetric lithography. The resist pattern is then used as a sacrificial template for atomic layer deposition (ALD), which upon removal can result in a porous nanolattice film. More information about the fabrication process is described in Supplement 1 A. The unit-cell geometry of the nanolattice is determined by the lithography step, where the 3D intensity patterns can be modeled by the Talbot effect. In this system the intensity patterns repeat along the z direction with the axial distance given by the Talbot distance z_t. The normalized Talbot distance is given by [40,41],

$$\frac{z_t}{\Lambda} = \frac{\gamma}{1-\sqrt{1-\gamma^2}} \tag{1}$$

where the parameter $\gamma = \lambda/n\Lambda$ is the normalized wavelength to the period ratio, λ is the wavelength of light used, n is the refractive index of the photoresist, and $\Lambda = D\sqrt{3}/2$ is the lattice period, with D as the diameter of nanospheres. The normalized Talbot distance is governed by the unitless γ parameter, which also influences the number of diffraction orders and sub-image planes generated. For $\gamma > 1/\sqrt{3}$, only 0^{th} and 1^{st} diffraction orders are propagating, resulting in simple periodic patterns without repeating sub-image planes. It can also be noted from Eq. (1) that at higher γ the normalized Talbot distance approaches unity and the axial and the lateral periods are similar ($z_t = \Lambda$), resulting in a more isotropic behavior. At lower γ, the axial period can be much larger than the lateral period ($z_t > \Lambda$), which can give rise to optical birefringence.

A more detailed model is performed using finite-difference time-domain (FDTD) method (ANSYS Lumerical) to predict the unit-cell geometry for different γ parameters, as illustrated in Fig. 2. In this simulation the intensity pattern is calculated for an array of nanospheres with 500 nm diameters illuminated with wavelength of 140 nm at normal incident angle, resulting in $\gamma = 0.2$. The simulation has periodic boundary conditions along the x and y directions and perfectly matched layer (PML) in the z direction. The simulated 2D and 3D views of the intensity patterns are shown in Fig. 2(a) and 2(b), respectively. From these patterns, a binary resist model

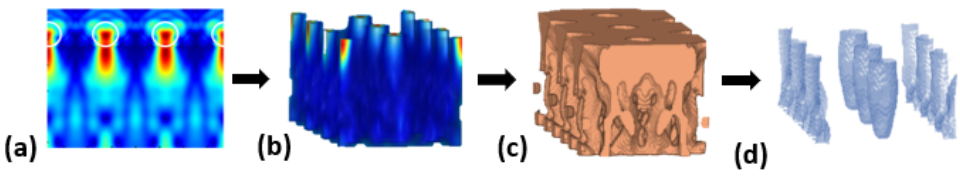

Fig. 2. Numerical modeling of lattices using FDTD at $\gamma = 0.2$. (a) 2D intensity pattern view obtained from FDTD monitor. (b) 3D Intensity profile of photonic interaction with resist. (c) Binary resist model utilized to replicate the exposure at threshold of 0.5, (d) surface extraction algorithm to mimic ALD to obtain thin-shell nanolattice post resist removal.

Optics EXPRESS

is used to predict the patterned photoresist structure, as shown in Fig. 2(c). In this model any photoresist regions exposed with intensity above a normalized intensity threshold value of 0.5 is assumed to be fully dissolved while regions below are unexposed, which predicts the resulting 3D structure. Finally, a shell extraction algorithm utilizes cells with the expected ALD thickness on all surface areas, thereby creating a thin-shell model as shown in Fig. 2(d).

Using the simulation models, nanolattices with different optical anisotropy can be designed for different γ. For illustrative purposes, the simulated nanolattice geometry for γ values of 0.2, 0.4, 0.6, and 0.8 are shown in Fig. 3, which corresponds to a constant sphere diameter of 500 nm exposed with 140, 280, 420, and 561 nm wavelength. The simulated intensity patterns along the x-z plane are shown in Fig. 3(a). The predicted thin-shell nanolattices using the binary resist model for the corresponding γ parameter are shown in Fig. 3(b). Note that the decrease in γ parameter again results in lattice geometry that is more anisotropic. The observed Talbot distances z_t from the FDTD model are 4.25, 2.05, 1.35, and 0.85 μm for γ parameter of 0.2, 0.4, 0.6, and 0.8, respectively, similar to the theoretical values of 4.29, 2.08, 1.30, and 0.87 μm using Eq. (1).

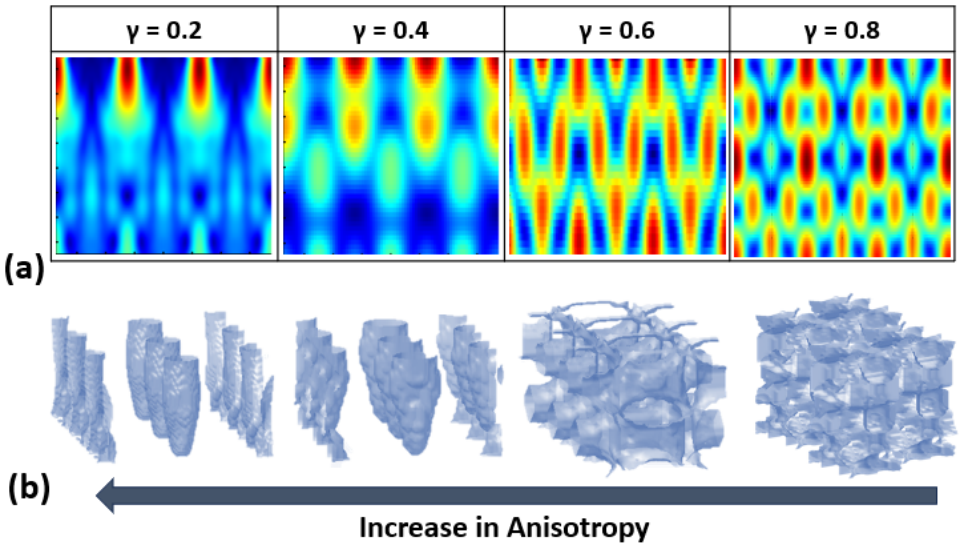

Fig. 3. (a) FDTD simulation of intensity distribution along the x-z plane of γ = 0.2, 0.4, 0.6, and 0.8, resulting in different unit-cell geometries. (b) Predicted nanolattice structures for the corresponding γ with 19.3 nm Al_2O_3 shell thickness.

The theoretical effective refractive indices and birefringence of the nanolattices can be modeled using FDTD by comparing the reflectivity of the structure to those from an anisotropic thin film. Here the nanolattice model consists of the simulated Al_2O_3 nanolattice, as illustrated in Fig. 3, with 800 nm height on silicon substrate. The anisotropic film model consists of a homogeneous film with unknown indices n_x, n_y, and n_z. The initial values of refractive indices are set to the same constant value of 1.0424, which is obtained an isotropic material model constructed in our previous work [12]. For both nanolattice and thin-film models, a planar wave with wavelength of 325 nm is directed along the z-axis at incident angles of 0° to 90°for both TE and TM polarizations. The boundary conditions are set to have Bloch wave for both x and y directions and PML for the z direction. The reflectivity along different angles of incidence for the nanolattice structure is first simulated, which serves as the reference. The n_x, n_y, and n_z of the anisotropic thin-film model are then updated iteratively until the resultant reflectivity matches those of the nanolattice structure. The convergence of the two models indicates that

Optics EXPRESS

the anisotropic thin-film model accurately captures the effect of the birefringent nanolattice structures. The final indices are reported as the calculated refractive index predicted using FDTD model, as described in subsequent sections.

2.2. Fabrication of birefringent nanolattices with low refractive index

The birefringent nanolattices are fabricated using 100 mm silicon substrates, which are coated with 100 nm of antireflection coating (ARC) (i-con-16, Brewer Science) to reduce back reflection. An 800 nm thick layer of positive-tone photoresist (PFi-88A2, Sumitomo Chemical) is coated using spin-coating. Polystyrene spheres with varying diameters of 390, 500 and 750 nm are assembled on the photoresist using Langmuir-Blodgett transfer method. The polystyrene nanospheres (2.5% aqueous solution, Polysciences) form a monolayer of hexagonally closed packed structures, which acts as a near-field phase mask for lithography. The photoresist is exposure using a HeCd laser with wavelength of 325 nm and a nominal dose of 90 mJ/cm^2. Post lithography, the nanospheres are removed by ultrasonication in deionized water, followed by development (Microposit CD-26).

The fabricated 3D photoresist nanostructures are used as template for conformal deposition using ALD (Savannah TM 200, Cambridge). Trimethyl aluminum and de-ionized water are used as precursors and half-reactions between these precursors result in formation of a self-limiting layer of Al_2O_3 over the 3D resist pattern. The samples are deposited with differing number of cycles of ALD, to investigate the influence of shell thickness on the refractive indices. Each cycle deposits about 1.1 angstrom of Al_2O_3. Post ALD process, the samples are subjected to thermal desorption in a temperature-controlled furnace to 550°C.

The fabricated nanolattice structures are shown in Fig. 4. Here the cross-sectional scanning electron microscope (SEM) images of the fabricated samples using 390, 500, and 750 nm are shown in Fig. 4(a)-(c), corresponding to for $\gamma = 0.59$, 0.46 and 0.31, respectively. The unit-cell

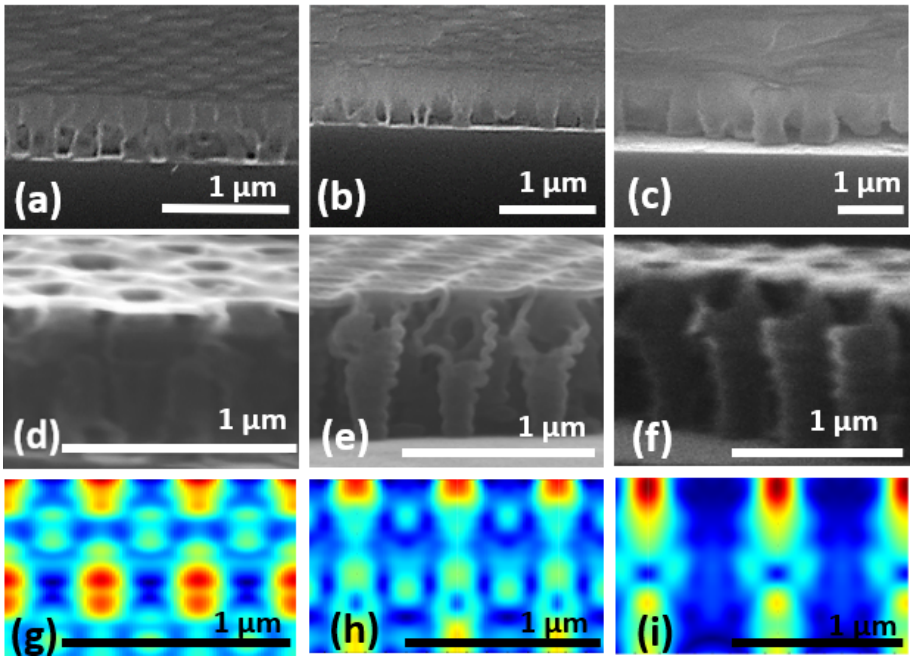

Fig. 4. Cross section SEM images of (a) 390 nm ($\gamma = 0.59$) (b) 500 nm ($\gamma = 0.46$), and (c) 750 nm spheres ($\gamma = 0.31$) with 800 nm resist height. Higher magnification images of (d) $\gamma = 0.59$ (e) $\gamma = 0.46$, and (f) $\gamma = 0.31$. Simulated intensity patterning using FDTD for (g) $\gamma = 0.59$, (h) $\gamma = 0.46$, and (i) $\gamma = 0.31$.

Optics EXPRESS

geometries of the different nanolattices are shown in the higher-magnification images depicted in Fig. 4(d)-(f). Here it can be observed that the nanolattice with lower $\gamma = 0.31$ is more cylindrical and is expected to exhibit a higher degree of anisotropy, as shown in Fig. 4(f). On the other hand, the unit-cell geometry for $\gamma = 0.59$ is more isotropic with a more uniform distribution of material in the out-of-plane and in-plane directions, as shown in Fig. 4(d), which confirms that the increase in γ parameter results in anisotropy. It is also observed that the intensity profiles of the samples from design and experimental results match closely, as observed from Fig. 4(g)-(i). It is important to note that while marginal variations in lattice heights can be observed, there are no systematic collapse of the nanolattices.

The normalized Talbot distance of the fabricated structures is plotted vs the γ parameter, as shown in Fig. 5. In can be noted that as γ decreases, the lattice geometry becomes more elongated in the depth direction. The Talbot distance can be experimentally determined by observing the repetitive patterns in the SEM images. For images with resist thickness less than z_t, the distance between fractional-image planes can be noted and multiplied to obtain the Talbot distance. Though this leads to a high error bar, the experimental trends match well with the FDTD models as shown from Fig. 5.

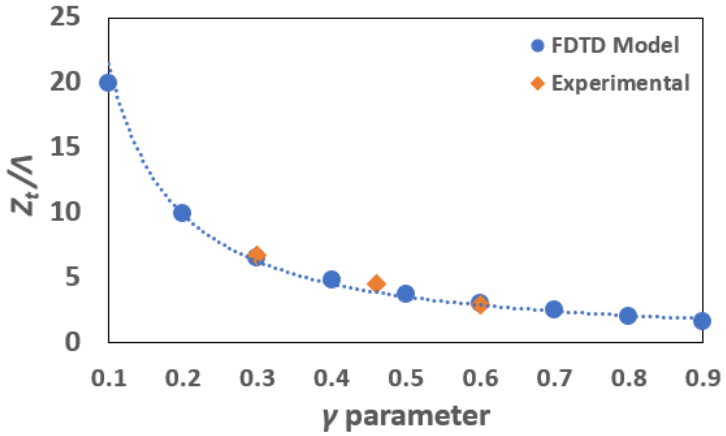

Fig. 5. The normalized Talbot distance vs γ parameter for the fabricated nanolattice samples (standard deviation of 0.00023). The predicted values using the analytical and FDTD models are also shown.

2.3. *Experimental characterization of nanolattice birefringence*

The optical properties of the nanolattices are characterized using spectroscopic ellipsometry (JA Woolam ellipsometer-M-2000DI). To model birefringent behavior accurately, a biaxial Cauchy model is used to describe the refractive indices $n_x(\lambda)$, $n_y(\lambda)$, and $n_z(\lambda)$. This model results in three identical Cauchy models that will describe the indices along orthogonal directions, which are simultaneously fitted for. For comparison, the index of the film was also measured using an isotropic model of the film with a single Cauchy material model along all three directions, namely $n_x(\lambda) = n_y(\lambda) = n_z(\lambda)$. The nanolattice film is characterized by a 450 to 1650 nm wavelength at incident angles of 40 to 70 degrees. The MSE values tend to vary between 11.7 and 27.3, indicating convergence of the calculated index values, and these samples were measured at 10 different spots to obtain a standard deviation of 2.3×10^{-4} over a single sample. More details of the ellipsometer measurements and uncertainty are described in Supplement 1 B.

Optics EXPRESS

3. Results and discussion

3.1. Ellipsometry characterization for anisotropic Cauchy behavior for nanolattices

The measured n_x, n_y, and n_z for the nanolattice samples are shown in Fig. 6. Here the nanolattice sample has $\gamma = 0.31$ and with 213 cycles of ALD, corresponding to 19.3 nm shell thickness. The measured indices using the isotropic and anisotropic Cauchy models at different incident angles are shown in Fig. 6(a) and 6(b), respectively. It can be noted from Fig. 6(a) that an increase in incident angle changes the measured index, indicating that the material is sensitive to the light polarization direction and that the isotropic model is not accurate. On the other hand, the measured indices using the anisotropic model changes less with incident angles, as shown in Supplement 1 B. The standard deviation of the indices at 633 nm for 30, 40, 50, 60, and 70 degrees is measured to be 5.4×10^{-5} for the anisotropic model, whereas it is almost two orders of magnitude higher at 2.0×10^{-3} for the isotropic model. It is noted that the measured n_x and n_y are very similar and within 1×10^{-5} of each other. This result indicates that the index is the same in the in-plane directions, which is expected given the hexagonal symmetry of the structure. Moreover, from the insert of Fig. 6(b), it can be noted that the n_z values are marginally higher than $n_x = n_y$ values, thereby indicating that the nanolattice behaves as a positive uniaxial crystal.

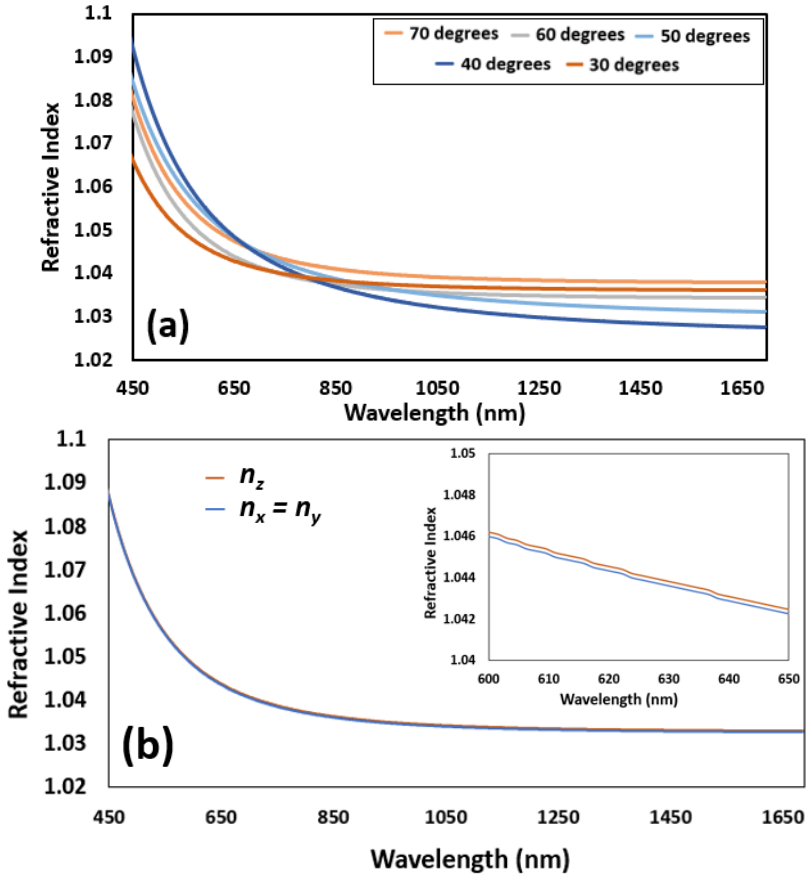

Fig. 6. Measured refractive indices vs wavelength for different angles of incidence for $\gamma = 0.31$ using (a) Cauchy isotropic (standard deviation of $2{\times}10^{-3}$) and (b) anisotropic models (standard deviation of $5.4{\times}10^{-5}$). The insert in (b) shows the birefringence observed over a range of wavelengths with two distinct indices along the in-plane and out-of-plane directions (red and blue lines).

Optics EXPRESS

The measured indices for all the fabricated nanolattices with various γ versus wall thickness are plotted in Fig. 7(a). It can be noted that as the number of cycles of ALD increases, there is a corresponding increase in the measured indices for all γ. Moreover, an increase in the γ parameter for a constant shell thickness results in an increase in the refractive index. Both trends can be attributed to the increased volume fraction of deposited Al_2O_3 for nanolattices with smaller periods. It can also be noted that the n_z values are marginally greater than $n_x = n_y$.

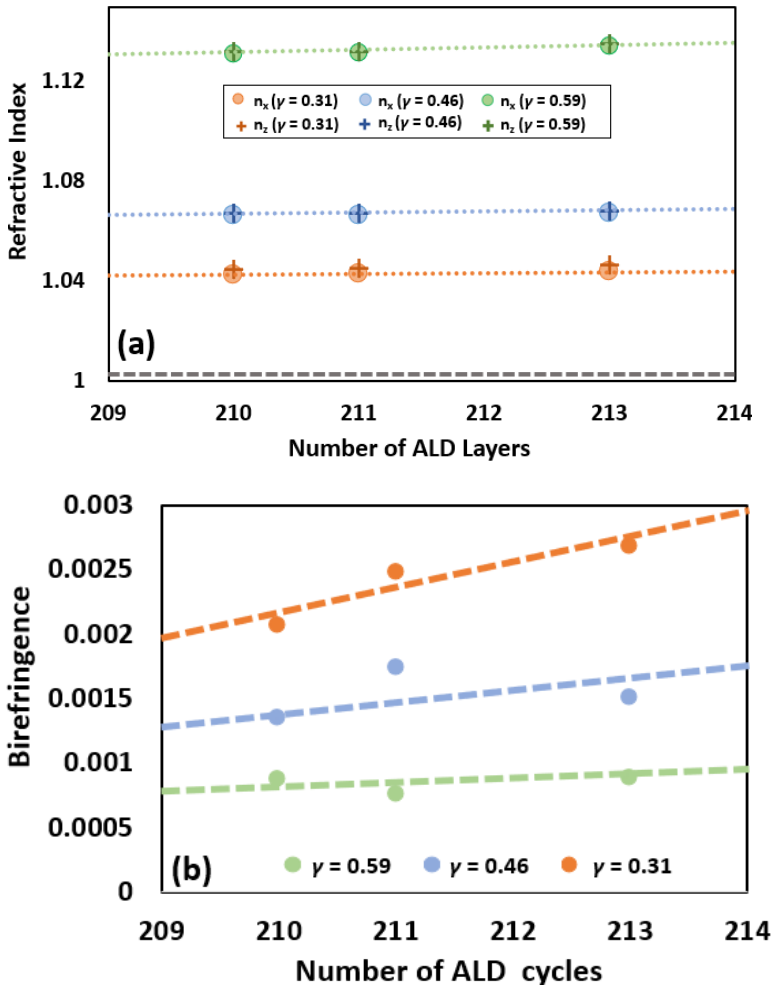

Fig. 7. (a) Variation of birefringent refractive indices with number of cycles of ALD for different periodicities (standard deviation of 0.00023). (b) Influence of periodicities and number of cycles of ALD on birefringence of nanolattices. The dotted lines represent the model with reflection convergence for birefringence using FDTD.

The birefringence can be calculated as $\Delta n = n_z - n_x$, as shown in Fig. 7(b). It can be noted from this result that the reduction in γ results in higher birefringence, reaching a maximum $\Delta n = 0.0026$ for $\gamma = 0.31$ at 213 ALD cycles. Moreover, the increase in shell thickness of low γ samples results in an increase in birefringence, as seen from the trend fit for $\gamma = 0.31$. However, there is no significant change in birefringence observed when the shell thickness is increased for $\gamma = 0.59$. The variation of birefringence versus γ can also be observed from Fig. 5(d), wherein the cross section of $\gamma = 0.59$ appears more isotropic, compared to cylindrical structures from the

Optics EXPRESS

cross section of Fig. 5(f) representing $\gamma = 0.31$. It is important to the measured birefringence is small given the low index nature of the nanolattice and can be potentially increased at lower porosity. An alternative method for birefringence calculation using FDTD is by extracting the relative phase of the transmitted electric fields below the nanolattice. The calculated birefringence using this method agrees with the reflection model with a maximum deviation of 3×10^{-4}, as detailed in Supplement 1 Section D.

The relationship between the nanolattice birefringence and γ parameter is established in Fig. 8. The orange data points indicate the experimental data obtained from spectroscopic ellipsometry for the γ values of 0.59, 0.46, and 0.31, which are exponentially fitted by the dotted line. The predicted birefringence using the FDTD model is also illustrated and matches closely to the experimental data. Here it can be observed that the birefringence increases at lower γ values, which can be attributed to higher structure period in the out-of-plane vs in-plane directions. This is reflected in the normalized Talbot distance, z_T/Λ, as shown in Eq. (1). This data indicates that the birefringence in nanolattices can be controlled by designing the lattice geometry.

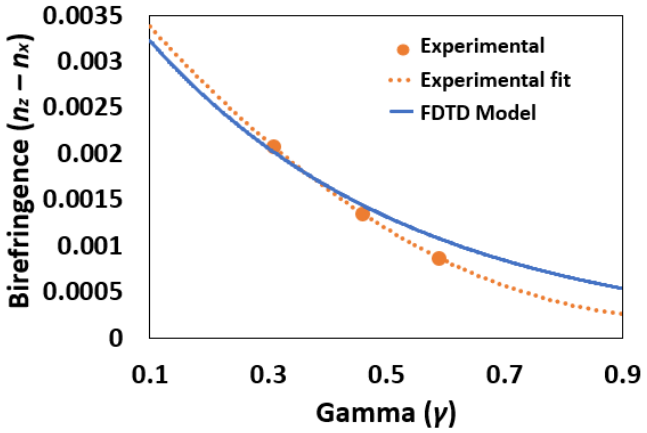

Fig. 8. Variation of birefringence with change in gamma parameter at 213 cycles of ALD.

3.2. *Reflectivity analysis of birefringent nanolattice film*

The measured and modeled reflectivity of the nanolattice film for $\gamma = 0.31$ at different incident angles are shown in Fig. 9. The experimental data is measured using a 633 nm laser linearly

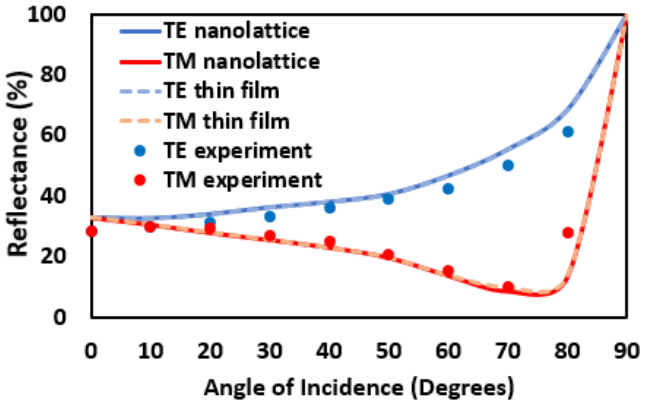

Fig. 9. Measured and predicted reflectivity versus different angles of incidence for $\gamma = 0.31$.

Optics EXPRESS

polarized in TE and TM modes at different angles of incidence and compared with the thin-film and nanolattice models calculated using FDTD methods, as discussed earlier. It was noted that an increase in reflected power results in corresponding increase in angle of incidence for the nanolattice for TE polarized light till it reached 100% reflectance at near-90-degree incidence angle. Whereas for TM polarized light, the reflectance values reached a minimum at Brewster angle, followed by a rapid increase to 100% at near-90-degree incidence angle. This trend can be observed in the experimental results, which match both models well. Some errors can be observed at higher incident angles, which can be attributed to the defects in the nanolattice samples using the larger laser spot footprint on the samples. Moreover, the predicted indices from the models can vary from the experimental data due to the non-systematic structural collapse, formation of cracks, aggregation of nanospheres, and dust particle deposition. All these defects cause a change in volume fraction in the nanolattice, resulting in variation of the experimental data to the models.

4. Conclusion

This research presents the design, modeling and fabrication of nanolattices with positive uniaxial birefringent behavior. The optical anisotropy depends strongly on the unit-cell geometry, which can be altered by varying the relatively periods in the longitudinal and axial directions as government by the γ parameter. The fabricated nanolattices with $\gamma = 0.31$, 0.46, 0.59 are characterized with spectroscopic ellipsometry using a biaxial Cauchy model and shows that the out-of-plane n_z is higher than the in-plane indices n_x and n_y, which are similar given the symmetry of the lattice. The refractive indices of the nanolattice can be predicted using FDTD methods and an iterative model, which match the experimental data well. It was noted that an increase in γ parameter resulted in reduction in optical anisotropy and the birefringence as well. The highest birefringence is measured for $\gamma = 0.31$, and has a value of 0.0026, for n_x =1.0438 and n_z =1.0465. In contrast, nanolattice with $\gamma = 0.59$ has the lowest birefringence of 0.0011, highlighting the important role γ plays in nanolattice anisotropy. This research demonstrates that anisotropy in nanolattices can be designed and can find applications in photonic integrated circuits, advanced AR/VR displays, and OLEDs.

Funding. National Science Foundation (CBET-2343526, TI-2314268); University of Texas at Austin.

Acknowledgments. This work was performed at UT Austin Texas Materials Institute (TMI), Nanomanufacturing System for mobile Computing and Energy Technologies (NASCENT), and Texas Nanofabrication Facilities, supported by grant CBET-2343526 and TI-2314268, and National Science Foundation (NSF) as part of the National Nanotechnology Coordinated Infrastructure (NNCI) grant NNCI-2025227.

Disclosures. The authors declare no conflicts of interest.

Data availability. Data underlying the results presented in this paper are available in Supplement 1.

Supplemental document. See Supplement 1 for supporting content.

References

1. B. C. Kress and I. Chatterjee, "Waveguide combiners for mixed reality headsets: a nanophotonics design perspective," Nanophotonics **10**(1), 41–74 (2020).
2. K.R. Curtis, "Unveiling magic Leap 2's advanced AR platform and revolutionary optics," *AR, VR, MR Industry Talks* Vol. 11932 (SPIE, 2022).
3. R. Gupta, R. Singh, A. Gehlot, *et al.*, "Silicon photonics interfaced with microelectronics for integrated photonic quantum technologies: a new era in advanced quantum computers and quantum communications," Nanoscale **15**(10), 4682–4693 (2023).
4. N. Yu and F. Capasso, "Flat optics with designer metasurfaces," Nat. Mater. **13**(2), 139–150 (2014).
5. A. V. Kildishev, A. Boltasseva, and V. M. Shalaev, "Planar photonics with metasurfaces," Science **339**(6125), 1289–1295 (2013).
6. F. Aieta, M. A. Kats, P. Genevet, *et al.*, "Multiwavelength achromatic metasurfaces by dispersive phase compensation," Science **347**(6228), 1342–1345 (2015).
7. N.I. Landy, S. Sajuyigbe, J.J. Mock, *et al.*, "Perfect Metamaterial Absorber," Phys. Rev. Lett. **100**(20), 207402 (2008).

Optics EXPRESS

8. J. B. Pendry, "Negative refraction makes a perfect lens," Phys. Rev. Lett. **85**(18), 3966–3969 (2000).
9. A. Zaidi, N. A. Rubin, M. L. Meretska, *et al.*, "Metasurface-enabled single-shot and complete Mueller matrix imaging," Nat. Photonics **18**(7), 704–712 (2024).
10. E. Yablonovitch, "Inhibited spontaneous emission in solid-state physics and electronics," Phys. Rev. Lett. **58**(20), 2059–2062 (1987).
11. S. John, "Electromagnetic absorption in a disordered medium near a photon mobility edge," Phys. Rev. Lett. **53**(22), 2169–2172 (1984).
12. Z. Qiang, W. Zhou, and R. A. Soref, "Optical add-drop filters based on photonic crystal ring resonators," Opt. Express **15**(4), 1823–1831 (2007).
13. M. Loncar, D. Nedeljkovic, T. Doll, *et al.*, "Waveguiding in planar photonic crystals," *Silicon-based and Hybrid Optoelectronics III*, Vol. 4293 (SPIE, 2001), pp. 94–99.
14. S. J. McNab, N. Moll, and Y. A. Vlasov, "Ultra-low loss photonic integrated circuit with membrane-type photonic crystal waveguides," Opt. Express **11**(22), 2927–2939 (2003).
15. I. Richter, P. C. Sun, F. Xu, *et al.*, "Design considerations of form birefringent microstructures," Appl. Opt. **34**(14), 2421–2429 (1995).
16. F. Xu, R. C. Tyan, P. C. Sun, *et al.*, "Fabrication, modeling, and characterization of form-birefringent nanostructures," Opt. Lett. **20**(24), 2457–2459 (1995).
17. S.S. Fedotov, A.S. Lipat'ev, T.O. Lipat, *et al.*, "Polarization-dependent birefringence in sodium aluminoborate glasses," Glass Ceram. **79**(3-4), 85–87 (2022).
18. J. Morikawa, A. Orie, T. Hashimoto, *et al.*, "Thermal and optical properties of the femtosecond-laser-structured and stress-induced birefringent regions in sapphire," Opt. Express **18**(8), 8300–8310 (2010).
19. L. Feng, L. Zhaowei, L. Vitaliy, *et al.*, "Form birefringence metal and its plasmonic anisotropy," Appl. Phys. Lett. **96**(4), 041112 (2010).
20. C. Yang and Y. Pochi, "Artificial uniaxial and biaxial dielectrics with the use of photoinduced gratings," J. Appl. Phys. **81**(1), 23–29 (1997).
21. P. T. Dang, J. Kim, and J. H. Lee, "Negative dispersion of a form birefringence in subwavelength gratings," Opt. Express **30**(11), 18287–18299 (2022).
22. D. Chen, M. L. V. Tse, and H. Y. Tam, "Optical properties of photonic crystal fibers with a fiber core of arrays of subwavelength circular air holes: Birefringence and dispersion," Prog. Electromagn. Res. **105**, 193–212 (2010).
23. J. Sung, M. Sukharev, E. M. Hicks, *et al.*, "Nanoparticle spectroscopy: birefringence in two-dimensional arrays of L-shaped silver nanoparticles," J. Phys. Chem. C **112**(9), 3252–3260 (2008).
24. N. J. Hutchinson, T. Coquil, A. Navid, *et al.*, "Effective optical properties of highly ordered mesoporous thin films," Thin Solid Films **518**(8), 2141–2146 (2010).
25. J. Q. Xi, J. K. Kim, E. F. Schubert, *et al.*, "Very low-refractive-index optical thin films consisting of an array of SiO2 nanorods," Opt. Lett. **31**(5), 601–603 (2006).
26. J. W. Leem, X.-Y. Guan, and J. S. Yu, "Tunable distributed Bragg reflectors with wide-angle and broadband high-reflectivity using nanoporous / dense titanium dioxide film stacks for visible wavelength applications," Opt. Express **22**(15), 18519–18526 (2014).
27. T. A. Schaedler, A. J. Jacobsen, A. Torrents, *et al.*, "Ultralight Metallic Microlattices," Science **334**(6058), 962–965 (2011).
28. D. Gailevičius, D. Paipulas, S. Hada, *et al.*, "Form birefringent polymeric structures realized by 3D laser printing," Opt. Lett. **48**(21), 5775–5778 (2023).
29. J. Paik, W. J. Feng, S. W. Clark, *et al.*, "Iridescent structural color by using ultra-low refractive index aerogel as optical cavity dielectric," Micro Nano Manuf. **1**(1), 1–12 (2024).
30. I. T. Chen, F. R. Poblete, A. Bagal, *et al.*, "Anelasticity in thin-shell nanolattices," Proc. Natl. Acad. Sci. U. S. A. **119**(38), e2201589119 (2022).
31. A. Bagal, X.A. Zhang, R. Shahrin, *et al.*, "Large-area nanolattice film with enhanced modulus, hardness, and energy dissipation," Sci. Rep. **7**(1), 9145–9154 (2017).
32. V. A. Premnath and C.-H. Chang, "Precise control of the optical refractive index in nanolattices," Opt. Lett. **48**(24), 6356–6359 (2023).
33. I. T. Chen, V. A. Premnath, and C.-H. Chang, "Multilayer dielectric reflector using low-index nanolattices," Opt. Lett. **49**(4), 1093–1096 (2024).
34. I. T. Chen, Z. Dai, D. T. Lee, *et al.*, "Fabrication of Non-Uniform Nanolattices with Spatially Varying Geometry and Material Composition," Adv. Mater. Interfaces **8**(17), 2100690 (2021).
35. X. A. Zhang, A. Bagal, E. C. Dandley, *et al.*, "Ordered 3D thin-shell nanolattice materials with near-unity refractive indices," Adv. Funct. Mater. **25**(42), 6644–6649 (2015).
36. M. Hirsch, P. Wierzba, and M. Jędrzejewska-Szczerska, "Tuning transfer function of fiber-optic Fabry–Pérot interferometer via introduction of birefringence in the cavity," Opt. Appl. **49**(2), 241–248 (2019).
37. V. A. Premnath, I. T. Chen, K. C. Chien, *et al.*, "Fabrication of three-dimensional opal nanolattices using template-directed colloidal assembly," J. Vac. Sci. Technol., B:Nanotechnol. Microelectron.:Mater., Process., Meas., Phenom. **40**(6), 062803 (2022).
38. I.T. Chen, E. Schappell, X. Zhang, *et al.*, "Continuous roll-to-roll patterning of three-dimensional periodic nanostructures," Microsyst. Nanoeng. **6**(1), 22 (2020).

Optics EXPRESS

39. C.-H. Chang, L. Tian, W. R. Hesse, *et al.*, "From two-dimensional colloidal self-assembly to three-dimensional nanolithography," Nano Lett. **11**(6), 2533–2537 (2011).
40. J. H. Min, X. A. Zhang, and C.-H. Chang, "Designing unit cell in three-dimensional periodic nanostructures using colloidal lithography," Opt. Express **24**(2), A276–A284 (2016).